On the Summertime Planetary Boundary Layer with Different Thermodynamic Stability in China: A Radiosonde Perspective✎

WANCHUN ZHANG, JIANPING GUO, YUCONG MIAO, AND HUAN LIU

State Key Laboratory of Severe Weather, Chinese Academy of Meteorological Sciences, Beijing, China

YU SONG

State Key Joint Laboratory of Environmental Simulation and Pollution Control, Department of Environmental Science, Peking University, Beijing, China

ZHANG FANG

Public Meteorological Service Center, China Meteorological Administration, Beijing, China

JING HE, MENGYUN LOU, YAN YAN, YUAN LI, AND PANMAO ZHAI

State Key Laboratory of Severe Weather, Chinese Academy of Meteorological Sciences, Beijing, China

ABSTRACT

Strongly influenced by thermodynamic stability, the planetary boundary layer (PBL) is key to the exchange of heat, momentum, and moisture between the ground surface and free troposphere. The PBL with different thermodynamic stability across the whole of China, however, is not yet well understood. In this study, the occurrence frequency and spatial distribution of the convective boundary layer (CBL), neutral boundary layer (NBL), and stable boundary layer (SBL) were systematically investigated, based on intensive summertime soundings launched at 1400 Beijing time (BJT) throughout China's radiosonde network (CRN) for the period 2012 to 2016. Overall, the occurrences of CBL, NBL, and SBL account for 70%, 26%, and 4%, respectively, suggesting that CBL dominates in summer throughout China. In terms of the spatial pattern of PBL height, a prominent north–south gradient can be found with higher PBL height in northwest China. In addition, the PBL heights of CBL and NBL were found to be positively (negatively) associated with near-surface air temperature (humidity), whereas no apparent relationship was found for SBL. Furthermore, clouds tend to reduce the occurrence frequency, irrespective of PBL type. Roughly 70% of SBL cases occur under overcast conditions, much higher than those for NBL and CBL, indicating that clouds govern to some extent the occurrence of SBL. In contrast, except for the discernible changes in PBL height under overcast conditions relative to those under clear-sky conditions, the changes in PBL height under partly cloudy conditions are no more than 170 m for both NBL and CBL types.

1. Introduction

The planetary boundary layer (PBL), the lowest layer of troposphere close to the surface, plays an important role in air pollution, weather, and climate (Garratt 1992, 1994; Stull 1988). The turbulent PBL is also the main place where the vertical exchange of momentum, heat, moisture, and atmospheric pollutants occurs between ground surface and free troposphere (e.g., Garratt 1992; Oke 2002; Hu et al. 2010; Zhang et al. 2015; Guo et al. 2016a). The turbulent motions in the PBL are responsible for the mixing processes in the atmosphere, which affects the vertical redistribution of moisture and momentum. This in turn impacts on the formation and evolution of boundary layer clouds such as stratocumulus and cumulus (e.g.,

Paluch and Lenschow 1991; Eltahir and Gong 1996; Amenu et al. 2005; Sherwood et al. 2014; Hirsch et al. 2017; Zhang et al. 2018).

The PBL is increasingly recognized as one of the important parameters that strongly influence the air quality (Guo et al. 2009; Sandip and Martial 2015; Li et al. 2017), partly account for the varying regional warming rate (Davy and Esau 2016), and significantly affect global weather and climate system (Medeiros et al. 2005; Esau and Zilitinkevich 2010; Fletcher et al. 2016; Solomon et al. 2017). Previous studies show that the heating and cooling of ground surface, cloudiness, and the variability in surface characteristics could affect the evolution of the PBL (e.g., Garratt 1994; Miao et al. 2015a, 2017). The PBL height during the daytime is found to be significantly negatively correlated with surface relative humidity but positively correlated with surface temperature (Zhang et al. 2013). Likewise, on the seasonal and annual time scales, the PBL height is positively associated with surface temperature and 10-m wind speed but negatively associated with surface pressure (Seidel et al. 2012; Guo et al. 2016b).

The PBL height is traditionally determined from the vertical profiles of temperature, humidity, and wind from atmospheric soundings. In addition, several other methods based on new data sources (e.g., lidar, Doppler radar, and sodar) have been developed to elucidate the PBL structure–processes (e.g., Holzworth 1964; Coulter 1979; Beyrich 1997; Steyn et al. 1999; Seibert 2000; Asimakopoulos et al. 2004; Hennemuth and Lammert 2006; Lammert and Bösenberg 2006; Dandou et al. 2009; Mao et al. 2009; McGrath-Spangler and Denning 2012; Chan and Wood 2013; Sawyer and Li 2013; Zhang et al. 2014; Guo et al. 2016b; Zhang et al. 2016).

Based on the atmospheric soundings collected in several major field campaigns, the diurnal variation of three dominant PBL types, namely, convective boundary layer (CBL), stable boundary layer (SBL), and neutral boundary layer (NBL) in the continental United States, were documented (Liu and Liang 2010): the CBL mainly occurs in the daytime with a peak at 1500 local time, in contrast to the SBL dominating at nighttime. Seidel et al. (2010) calculated the PBL height by applying seven common methods to the profiles of temperature, potential temperature, virtual potential temperature, relative humidity, specific humidity, and refractivity and found there existed large uncertainties with respect to various methods to estimate PBL height. Then the climatology of the PBL height over Europe and the continental United States were compiled using the bulk Richardson number method (Seidel et al. 2012). The same method has also been utilized by Guo et al. (2016b) to develop a radiosonde-based PBL height climatology in China, which exhibits large diurnal,

seasonal, and spatial variations. This could be at least in part in association with the strong variations in aerosol pollution in China (Guo et al. 2011, 2016c) and atmospheric thermodynamic stability (Tokinaga et al. 2006; Tang et al. 2016). Although the PBL height over China has been well characterized from spaceborne lidars (e.g., Liu et al. 2015; Zhang et al. 2016) and radiosondes (Guo et al. 2016b), most of the other PBL characteristics remain poorly understood, including the thermodynamic stability and its associated meteorological factors.

Since 2011, intensive radiosonde observational campaigns at 1400 Beijing time (BJT) in summer (May–June–July–August) have been performed at most sites of the newly updated L-band China Radiosonde Network (CRN) as operated by the China Meteorological Administration (CMA) (Guo et al. 2016b; Zhang et al. 2016). The afternoon soundings provide us a unique opportunity to look into the thermodynamic stability of PBL. Thus, one of the main objectives of this study is to unravel the occurrence frequency and spatial distribution of CBL, SBL, and NBL across China using long-term fine-resolution atmospheric soundings. Another objective is to understand the relationships between meteorological variables and PBL height that differs by three PBL types.

The rest of the present paper is organized as follows. Section 2 describes the data and method used in this study, as well as the uncertainty analysis for the PBL height retrievals. Section 3 presents the climatology of different PBL types in China and its association with other atmospheric variables. In section 4, detailed discussion with regard to the PBL height climatology and the potential influential factors on the development of PBL will be provided. Finally, the key findings are summarized in section 5.

2. Data and methods

a. Radiosonde and meteorological data

The L-band radiosondes of CRN are conventionally launched twice a day at 0800 and 2000 BJT, and additional soundings are made at 1400 BJT in summer (May–June–July–August) at most radiosonde sites mainly for improving the capability of predicting high-impact weather in China. The L-band radiosondes are produced by the Nanjing Daqiao Co., Ltd., and the Shanghai Changwang Meotech Co., Ltd. (Xu et al. 2007), which provide fine-resolution (1 s) profiles of temperature, humidity, wind speed, and wind direction (Guo et al. 2016b; Zhang et al. 2016). As the previous studies (Tao et al. 2006; Xing et al. 2009; Bian et al. 2011; Ma et al. 2011) pointed out, the accuracy of the temperature profiles within the lower portion of the

troposphere is similar to that of GPS RS92 radiosonde (produced by Vaisala), which is less than 0.1 K. Such good data accuracy provides us with enough confidence to investigate PBL climatology in China using these L-band soundings of CRN.

In this study, the characteristics of afternoon PBL during summer were investigated using the 1400 BJT soundings from 2012 to 2016 collected from CRN, owing to most of the exchanges of energy, moisture, and air pollutants occurring in the PBL in the afternoon (Garratt 1994; Guo et al. 2016b). Considering the time consistency, the near-surface meteorological observations from the collocated radiosonde sites are used to understand the factors governing the PBL development, including near-surface temperature T_{sfc}, near-surface relative humidity RH_{sfc}, near-surface pressure P_{sfc}, and 10-m wind speed WS_{10}. The former three meteorological factors were calculated by taking the average over the five lowest consecutive soundings starting from the ground surface, whereas WS_{10} was calculated by taking the average over the wind profiles from the second-lowest to third-lowest soundings.

Given the substantial difficulties and uncertainties in determining the PBL types caused by precipitation, the 1400 BJT sounding data have been excluded for the days when precipitation occurred from 1200 to 1400 BJT. Additionally, the sites that have less than 30 valid soundings at 1400 BJT from 2012 to 2016 are not considered. As a result, there are 5399 valid summertime soundings collected from the 92 radiosonde sites of CRN at 1400 BJT. The total cloud cover (CLD) data measured at 1400 BJT at the same radiosonde sites have been used, in addition to the hourly rain gauge measurements recorded at the hours from 1200 to 1400 BJT.

To understand the impacts of land surface processes on the development of PBL in the afternoon, the dataset from the Global Land Data Assimilation System (GLDAS; Rodell et al. 2004) was analyzed. The GLDAS contains a series of geophysical parameters reflecting the state of land surface (e.g., soil moisture and surface temperature) and flux (e.g., evaporation and sensible heat flux), based on four land surface models (CLM, Mosaic, Noah, and VIC). The surface sensible heat fluxes (SHF_{sfc}) and soil moisture fields in China derived from the Noah model (Chen and Dudhia 2001) were used as well.

b. Determination of PBL type

During the daytime, because of the sufficient solar radiation reaching the land surface, the CBL typically dominates over land, which can reach a few kilometers in the afternoon (Chen and Houze 1997). By contrast, when the surface cools by the nocturnal radiation

processes, the SBL takes over the bottom portion of the troposphere (Zhang et al. 2011; Miao et al. 2015b). The residual layer is neutrally stratified, resulting in turbulence that is nearly of equal intensity in all directions (Sivaraman et al. 2013; Blay-Carreras et al. 2014), referred to as the NBL.

Despite the dominance of CBL in the afternoon, the SBL and NBL may form under certain meteorological conditions (Medeiros et al. 2005; Poulos et al. 2002; Stull 1988). The complicated connections between the PBL structure and meteorology make it imperative that the PBL types be determined upfront.

Here the determination of PBL types is largely based on the methods developed by Liu and Liang (2010), where the soundings they used are at a vertical resolution of ~5 hPa, which is in sharp contrast to the vertical resolution of L-band radiosonde (~1 hPa) to be used in the present study. Therefore, subsample operation in the vertical has been performed by resampling five consecutive original 1-hPa measurements to one 5-hPa measurement. As such, a series of coarser-resolution soundings (5 hPa) are derived, and Fig. S1 is a case in point. Then, the PBL types were determined by calculating the near-surface potential temperature difference (PTD) between the fifth-lowest measurement and second-lowest measurement. The threshold value of PTD is set to be 0.1 K, and the thermodynamic stability of PBL has to be further determined using the bulk Richardson number based on the original lowest 100-m radiosonde measurements. Specifically, if the PTD lies between −0.1 and 0.1 K, the PBL is identified as NBL; if the PTD is higher than 0.1 K and the bulk Richardson number is positive, the PBL type is identified as SBL; and other PBL cases can be considered as CBL (Vogelezang and Holtslag 1996; Eresmaa et al. 2006; Tang et al. 2015).

c. PBL height estimation and uncertainty analysis

The estimation method of PBL height differs by varying PBL types. Similar to Liu and Liang (2010), the PBL height for both CBL and NBL is calculated as the height at which an air parcel rising adiabatically from the surface becomes neutrally buoyant (Stull 1988). Starting from the surface, the height where the gradient of potential temperature first becomes greater than a certain gradient threshold (GT) of potential temperature is considered as the estimated PBL height.

For the SBL, the determination of the PBL height is much more uncertain. Turbulence in the SBL can result from either buoyancy forcing or wind shear (Bonner 1968; Garreaud and Muñoz 2005). If both the stability-derived and wind shear–derived PBL heights are derived, the lowest is estimated to be the PBL height for SBL (Liu and Liang 2010; Sivaraman et al. 2013). Figure S2 (in
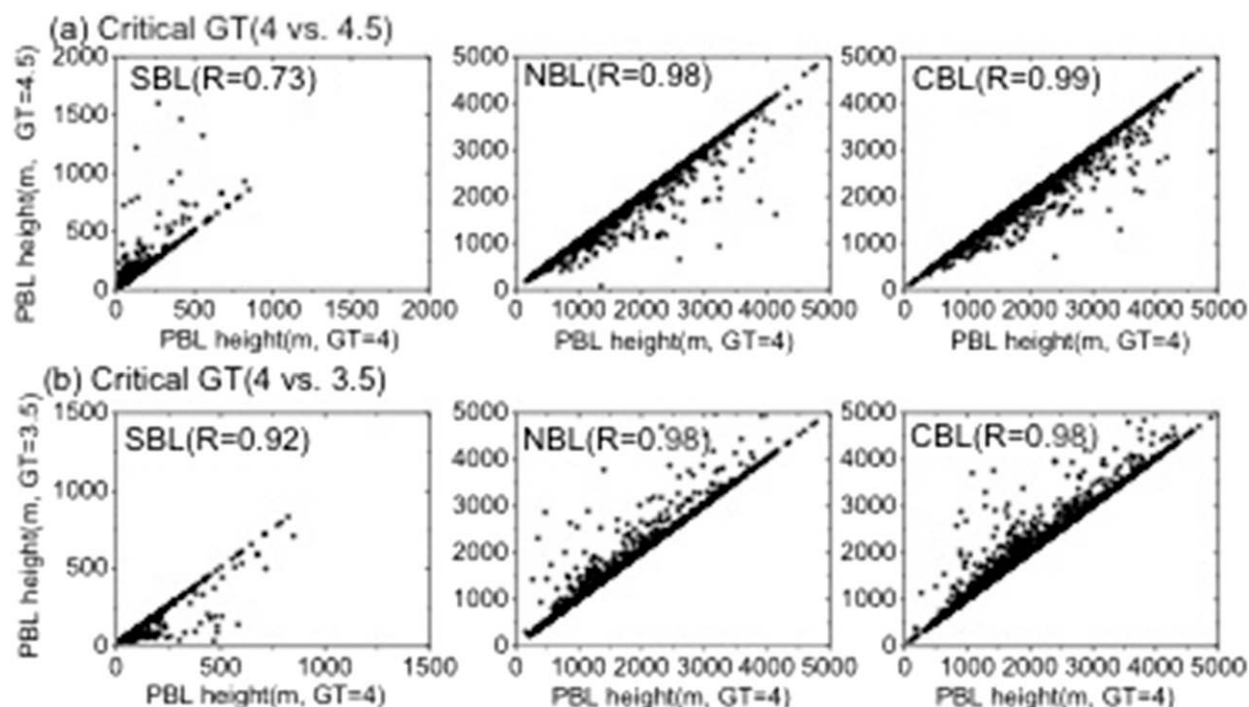
FIG. 1. Scatterplots showing (a) PBL heights computed using 4 K km^{-1} (on the x axis) and 4.5 K km^{-1} (on the y axis) as critical potential temperature GT for the (left to right) SBL, NBL and CBL. (b) As in (a), but with 3.5 K km^{-1} (on the y axis). The results are based on 5399 soundings across China in summer (May–August) from 2012 to 2016.

supplementary material file JCLI_D17231s1) illustrates the typical profiles of CBL, NBL, and SBL, and their corresponding PBL heights are 1650, 721, and 249 m above ground level (AGL), respectively.

To quantify the uncertainties in the estimation of PBL heights, sensitivity analysis by selecting various values of GT has been performed (Argentini et al. 2005). Figures 1a,b compared the PBL heights calculated using 3.5, 4, and 4.5 K km^{-1} as GT. As expected, the PBL heights of GT = 4.5 K km^{-1} (3.5 K km^{-1}) are generally higher (lower) than those of GT = 4 K km^{-1}. The heights of NBL and CBL based on different GT are significantly correlated with each other ($R = 0.98$). In contrast, the heights of SBL based on various GT have relatively weaker correlations with each other.

We further checked the changes in occurrence frequency of SBL, NBL, and CBL caused by the different critical GT values applied. The changes in their corresponding PBL heights were examined as well, which is summarized in Table S1 (in supplementary material file JCLI_D17231s1). Overall, the deviation of frequency for SBL, NBL, and CBL is less than 13%, and the changes in PBL heights is not more than 177 m, which could make sense for SBL cases. However, the uncertainties can be negligible for NBL and CBL, since most of their PBL heights are much higher.

3. Results

This section presents the basic climatology of three PBL types (i.e., SBL, NBL, and CBL). Comparisons of radiosonde-based PBL height climatology under different CLD conditions are made to elucidate the impacts of cloud on the development of PBL in the afternoon during the summer. Then we present comprehensive analysis results with regard to the correlations between PBL heights and four typical meteorological variables, including T_{sfc}, P_{sfc}, RH_{sfc}, and WS_{10}.

a. Climatology of PBL height for various PBL types

Figure 2 shows the frequency distribution and cumulative frequency distribution of PBL heights for SBL, NBL, and CBL. At 1400 BJT, 96% of SBL are lower than 500 m, while 83% (76%) of CBL (NBL) are higher than 1000 m. On the whole, all PBL heights estimated from soundings are lower than 5 km at 1400 BJT across China.

In terms of the numbers of valid soundings at each site at 1400 BJT during summer, the numbers of soundings at 69 sites (about 75%) range from 30 to 60 (Fig. 3). In particular, the valid soundings at Beijing (39.80°N, 116.47°E) and Shanghai (31.40°N, 121.48°E) are larger than 150. Figures 3b–d present the spatial distributions
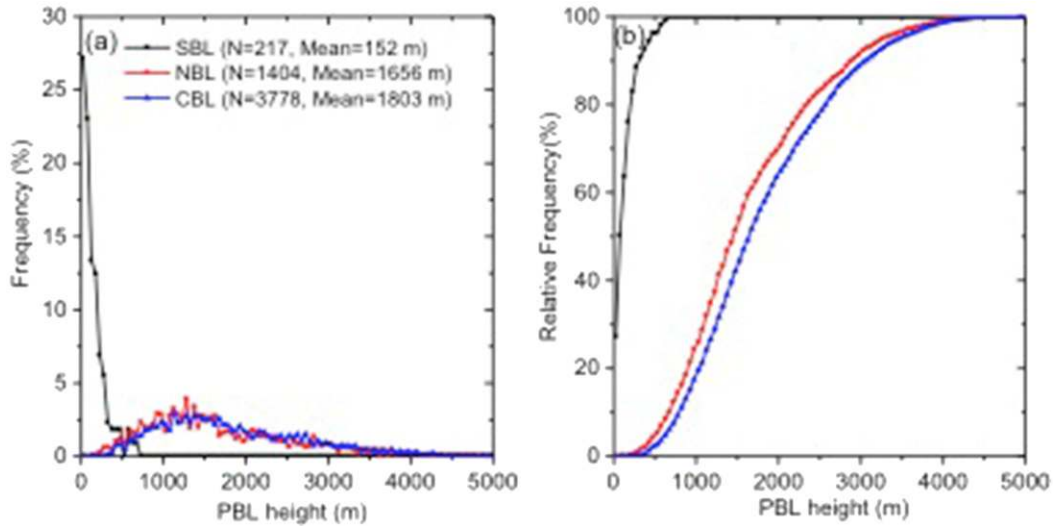
FIG. 2. (a) Frequency distribution and (b) cumulative frequency distribution of PBL heights for SBL (black), NBL (red), and CBL (blue) at 1400 BTJ in summer for the period of 2012–16. The number of soundings N and mean value at each observed time are also given.

of occurrence frequency with respect to CBL, NBL, and SBL at 1400 BJT across China, which on average are 70%, 26%, and 4%, respectively. The occurrence frequency of NBL is generally less than 40% at most sites of

CRN. By comparison, the CBL dominates over most sites of CRN.

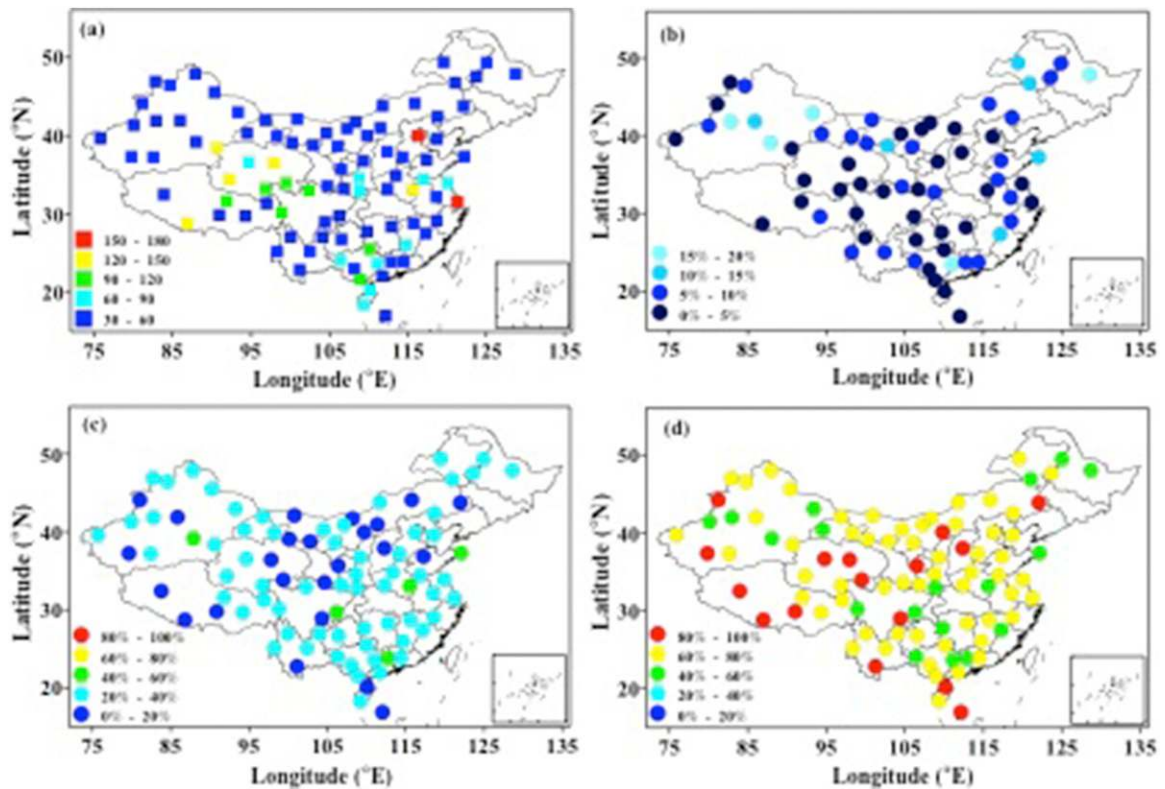Irrespective of PBL regimes, Fig. 4a displays the spatial distribution of mean PBL height at 1400 BJT in

FIG. 3. Spatial distributions of (a) number of soundings from CMA radiosonde sites: 150–180 (red), 120–150 (yellow), 90–120 (green), 60–90 (cyan), and 30–60 (blue). The frequency (percent) for PBL states classified by atmospheric stability: (b) SBL [15%–20% (light cyan), 10%–15% (dark cyan), 5%–10% (blue), and 0%–5% (black)]; (c) NBL [80%–100% (red), 60%–80% (yellow), 40%–60% (green), 20%–40% (cyan), and 0%– 20% (blue)]; (d) as in (c), but for CBL, at 1400 BJT in summer for the period of 2012–16.
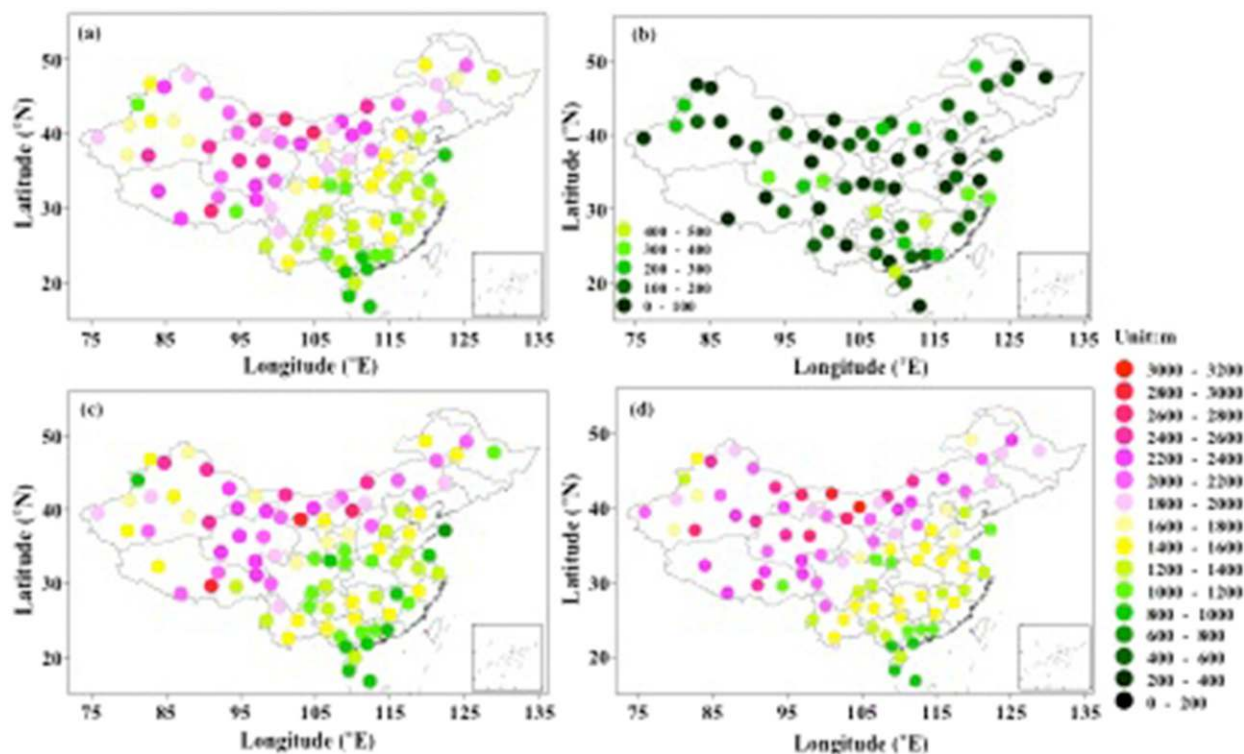
FIG. 4. Spatial distribution of mean PBL height (m) for (a) all types, (b) SBL, (c) NBL, and (d) CBL at 1400 BJT in summer for the period of 2012–16. The 16-color scale is black for 0–200 m and dark red for 3000–3200 m in increments of 200 m.

China. The averaged PBL height of all sites is 1694 m AGL, indicative of high tendency of well-developed PBL in the afternoon. A prominent north–south PBL height gradient is found, with higher PBL height in northwestern China, which is consistent with spatial pattern revealed by previous PBL studies derived from the Cloud–Aerosol Lidar with Orthogonal Polarization (CALIOP) on board *CALIPSO* (Huang et al. 2009; Liu et al. 2015; Zhang et al. 2016). The climatological PBL height in northwest China is generally greater than 1800 m AGL, whereas the values are usually less than 1400 m AGL over southeast and coastal areas. The high soil moisture may be one of the causes accounting for the relatively shallower daytime PBL over the east coast (McGrath-Spangler and Denning 2012; Wang and Wang 2014, 2016). In contrast, the low soil moisture in the north and west regions tends to favor the PBL development by partitioning more solar radiation to sensible heat flux (Wang and Wang 2014).

Figures 4b–d illustrate the spatial distributions of PBL height of SBL, NBL, and CBL. Specifically, Fig. 4b shows that the PBL height for SBL is merely 152 ± 100 m AGL (mean value ± standard deviation). However, the values increase sharply to 1656 ± 562 m AGL for NBL and 1803 ± 550 m AGL for CBL (Figs. 4c,d). In other words, the mean PBL heights tend to be on average

reduced by ∼150 m in the presence of NBL as compared with those for CBL. Although the SBL develop more frequently after sunset, which can also be established during the daytime under certain synoptic conditions.

To reveal the spatial discrepancy in PBL, we further selected six typical regions of interest (ROIs, defined and shown in Fig. S3 in supplementary material file JCLI_D17231s1), including 1) the North China Plain (NCP), 2) the Yangtze River Delta (YRD), 3) the Pearl River Delta (PRD), 4) the Taklimakan Desert (TKD), 5) the Tibetan Plateau (TBP), and 6) the Sichuan basin (SCB). The occurrence frequency and averaged PBL height of CBL, NBL, and SBL at these six ROIs are illustrated in Fig. 5 and Table 1. Except for PRD, in which the 1400 BJT soundings were only launched in May and June, the 1400 BJT soundings in other ROIs are all launched throughout the whole summer season (June–July–August).

Overall, the CBL occurs most frequently in summer (60%), about 2 times higher than the frequency of NBL (less than 30%), let alone the frequency of SBL (less than 10%). Among these six ROIs, the TBP has the highest occurrence frequency of CBL (Fig. 5), characterized by an averaged PBL height of 2222 m AGL (Table 1). Although both PRD and TKD have similar
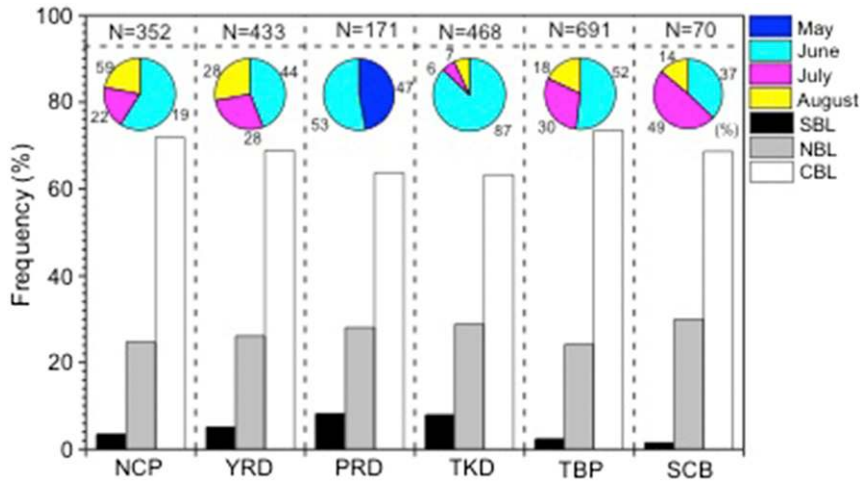
FIG. 5. The occurrence frequency of SBL, NBL, and CBL in six ROIs: NCP, YRD, PRD, TKD, TBP, and SCB, at 1400 BJT during in summer (May–August) for the period of 2012 to 2016, respectively. The bars show the frequency of different PBL types [SBL (black), NBL (gray), and CBL (white)]. The pie charts show the frequency percentage distribution for each month.

occurrence frequencies for all the three PBL types, the mean PBL heights are quite different, which are 1067 and 2248 m AGL for PRD and TKD, respectively (Table 1). This large difference in PBL height over PRD and TKD could be relevant to the large discrepancy of RH_{sfc} and SHF_{sfc}. The mean RH_{sfc} over PRD and TKD is 50% and 22%, respectively, whereas the mean SHF_{sfc} is 113 and 290 W m^{-2} at these two ROIs. In the afternoon, less moisture in the PBL of arid TKD is associated often with lower RH and higher SHF, which generally facilitates the development of PBL (Stull 1988; Liu et al. 2004; Dirmeyer et al. 2014). This could be likely the main reason why the high PBL height occurred in TKD rather than in PRD.

b. The potential impact of cloud on the development of various PBL regimes

It is well known that clouds alter the solar radiation reaching the land surface, which further modulates the PBL in the afternoon. Figure 6 shows the mean PBL height and frequency for SBL, NBL, and CBL under different CLD conditions. It is intriguing to note that the PBL height does not change much when CLD ranges from 0% to 80%, no matter what the PBL regime is.

Only when the CLD becomes higher than 80%, which is referred to as the overcast condition, the PBL height for SBL, NBL and CBL decreases by a certain magnitude. As compared with that under clear-sky conditions (CLD < 20%), the averaged PBL height at 1400 BJT under overcast conditions decreases by ~400 and ~300 m for NBL and CBL, respectively. In contrast, the depth of SBL keeps almost constant. Relative to PBL under clear-sky condition, the changes in PBL height under partly cloudy conditions are less than 170 m for both NBL and CBL regimes (Table S2).

Figure 6b shows the occurrence frequency of SBL, NBL, and CBL under different CLD conditions in summer. In general, the occurrence frequency of CBL is higher than 40% under overcast conditions, almost twice the frequency under clear-sky conditions. Similarly, the occurrence frequencies of NBL are ~20% and ~50% for the clear-sky and overcast conditions, respectively. For SBL, the occurrence frequency is merely ~10% under clear-sky conditions, as compared to ~70% under overcast conditions. Such huge differences existing in the occurrence frequency of CBL, NBL, and SBL suggested that the CLD could play a significant role in modulating the development of PBL. The presence of

TABLE 1. The statistics of mean value and standard deviation (sd) of PBL heights (m AGL) for SBL, NBL, and CBL in six ROIs: the NCP, YRD, PRD, TKD, TBP, and SCB at 1400 BJT in summer (May–June–July–August) for the period of 2012 to 2016.

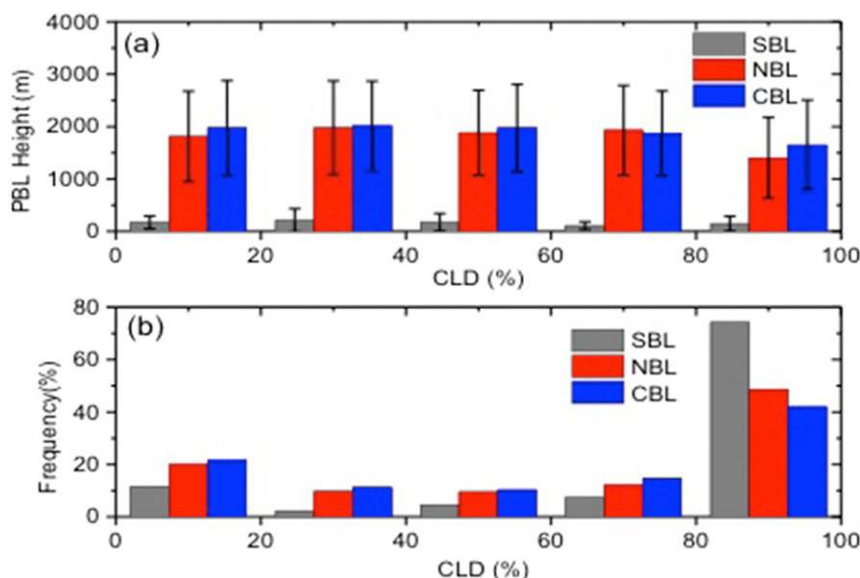|	NCP mean (sd)	YRD mean (sd)	PRD mean (sd)	TKD mean (sd)	TBP mean (sd)	SCB mean (sd)
SBL	109 (110)	199 (184)	174 (163)	114 (98)	211 (197)	—
NBL	1529 (712)	1241 (455)	999 (330)	1982 (1020)	2188 (752)	1300 (338)
CBL	1703 (739)	1297 (474)	1067 (365)	2248 (1004)	2222 (751)	1317 (409)

FIG. 6. Bar charts showing (a) the mean PBL height and (b) the occurrence frequency for three PBL types: SBL (gray), NBL (red), and CBL (blue) under different cloud cover (CLD) conditions (with a bin size of 20%) in summer for the period of 2012–16. Note that the error bars in (a) denote the standard deviations of PBL height.

clouds tends to reduce the solar radiation reaching the surface in the afternoon and thus weaken the vertical turbulent mixing, which in turn suppresses the PBL development (Li et al. 2017). Therefore, a reduced PBL height typically ensues (Wetzel et al. 1996; Freedman et al. 2001; Zhou and Geerts 2013).

To figure out the spatial distribution of potential cloud influences on CBL, 29 radiosonde sites evenly scattered across the China were selected, in which the number of valid CBL sounding is more than 30 for both overcast and clear-sky conditions. As shown in Fig. 7, one noticeable feature is that the PBL height under clear-sky conditions is systematically lower than that under overcast conditions throughout all these 29 sites, even though the PBL height under both conditions ranges from 800 to 2600 m. On average, the difference of mean PBL height is 336 m, as indicated in Fig. 7c.

c. Relationships between PBL height and meteorological variables

In this section, we will analyze the relationships between PBL height and several meteorological parameters, including T_{sfc}, RH_{sfc}, P_{sfc}, and WS_{10}. To better understand the development of SBL in the afternoon, the meteorological factors for the days with SBL were compared with those with CBL, including CLD, T_{sfc}, RH_{sfc}, WS_{10} and SHF_{sfc}. Comparing with the CBL regime, the SBL tends to be formed under the meteorological conditions characterized by relatively high CLD and RH_{sfc}, and low T_{sfc}, WS_{10}, and SHF_{sfc} (Fig. 8).

Figure 9 shows the correlation coefficient R of PBL height and various meteorological factors in the six ROIs for different PBL regimes, and the gray shaded areas indicate the R values are statistically significant at the 95% confidence level. Typically, the PBL height is positively correlated with T_{sfc} in six ROIs for both NBL and CBL, including the NCP ($R = 0.37$, 0.25 for NBL and CBL, respectively), YRD ($R = 0.55$, 0.62), PRD ($R = 0.73$, 0.66), SCB ($R = 0.68$ under CBL), and TBP ($R = 0.19$, 0.24), and the lowest correlation ($R = 0.02$, 0.13) is found in TKD. For SBL, only the correlation of the YRD region show here ($R = -0.30$). More details on the correlations can be found in Table S3.

In contrast, negative relationships are observed between the PBL height and RH_{sfc} in summer for NBL and CBL (Fig. 9), and the R values are mostly lower than -0.6 except for those in TKD ($R = -0.39$ for NBL, -0.51 for CBL) regions. By comparison, the positive correlations ($R = 0.36$) in TKD between PBL height and RH_{sfc} are found in summer for SBL. For a specific location, the high RH_{sfc} may be associated with high soil moisture and high latent heat flux, which will inhibit the occurrence of convection and turbulence within SBL and thus lead to a relatively deeper SBL. For CBL and NBL, higher T_{sfc} and lower RH_{sfc} have been found to be linked to more sensible heat fluxes, favoring the development of PBL during the daytime (Zhang et al. 2013).

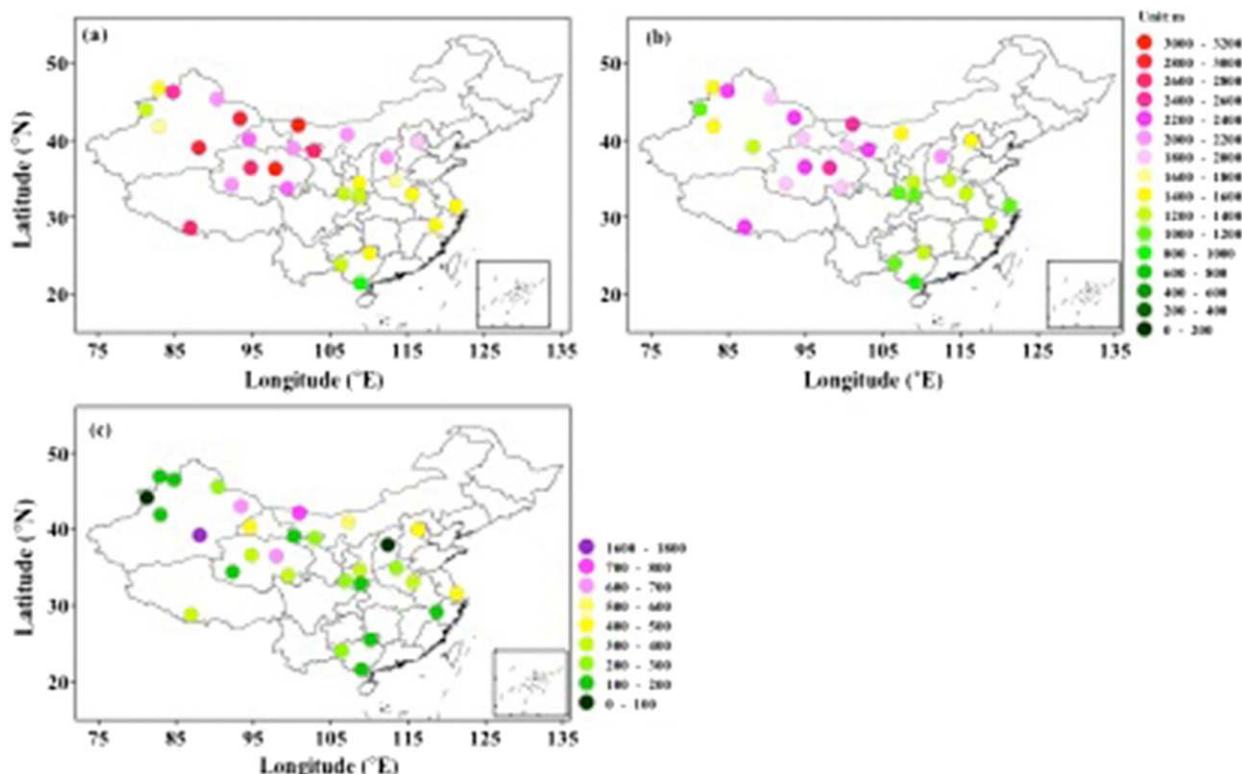In addition, the relationships are ubiquitously negative between the PBL height and P_{sfc} in summer for

FIG. 7. The spatial distributions of mean PBL heights (m) at 1400 BJT in summer for the period 2012–16 for CBL days under (a) clear-sky ($0\% \leq$ CLD $\leq 20\%$) and (b) overcast conditions ($80\% \leq$ CLD $\leq 100\%$); the 16-color scale is black for 0–200 m and dark red for 3000–3200 m in increments of 200 m. (c) The spatial distribution with respect to the differences of PBL heights between clear-sky and overcast conditions; the 9-color scale is black for 0–100 m and dark purple for 900–1000 m in increments of 100 m.

CBL, NBL and SBL. Similar correlation analyses using WS_{10} show that these parameters are not significantly correlated with PBL height at 1400 BJT in summer.

4. Discussion

Regarding the large discrepancy in PBL height in PRD and TKD (Fig. 5), it is known that PRD is characterized by richer vegetation cover compared with TKD; the relatively strong surface evaporation in PRD can substantially increase the near-surface humidity and lead to less surface sensible heat flux, which suppresses the PBL height over PRD (Zhang et al. 2013; Dirmeyer et al. 2014).

In addition to the local-scale atmospheric processes, the large-scale synoptic conditions have been well recognized to be able to govern the development of the PBL (Whiteman and Doran 1993; Garratt 1994; Hoover et al. 2015; Miao et al. 2017). For example, the subsidence associated with the high pressure systems (e.g., anticyclone) may suppress the development of PBL, while the large-scale upward motions induced by the low pressure systems (e.g., fronts, cyclone) would

favor the growth of PBL (Stull 1988). Specifically, the cold front passage generally comes with CBL, since the strong winds within PBL would favor the development the PBL dynamically. In contrast, sometimes the presence of warm front could facilitate the formation of SBL, since warm air mass behind the front would climb over the local colder air, leading to an increase in atmospheric stability and a suppressed growth in PBL to some extent (Keyser and Anthes 1982; Stull 1988; Sun et al. 2002). Conversely, the stable PBL is also favorable for the low-level stratus cloud formation and maintenance (Lin et al. 2016).

Furthermore, clouds (especially under overcast condition) are generally associated with lower PBL height (Fig. 6). As shown in Fig. 10, compared with the negligible association between CLD and WS_{10}, high CLD was found to be associated with low T_{sfc} and higher RH_{sfc} (Betts et al. 2017; Garcia-Carreras et al. 2017), which was also accompanied with the lower PBL height in the afternoon (Zhang et al. 2013). Although high wind speed is recognized to be positively associated with annual averaged PBL height in the morning or afternoon (Guo et al. 2016b), this positive relation cannot be
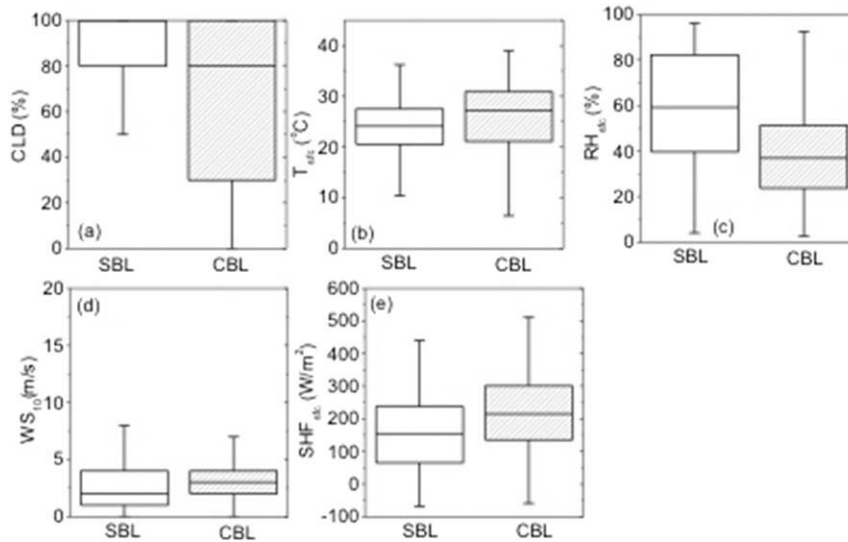
FIG. 8. Box plots comparing meteorological: (a) CLD, (b) surface temperature T_{sfc}, (c) relative humidity RH_{sfc}, (d) 10-m wind speed WS_{10}, and (e) surface sensible heat flux SHF_{sfc} between the days with SBL and those with CBL, as averaged over 67 radiosonde sites with valid SBL observations.

apparently seen from the afternoon PBL during summer. There may exist complicated coupling effects between the near-surface meteorological factors, CLD, and PBL in the afternoon. For instance, high CLD is often associated with high RH_{sfc} and low PBL height, owing to the modulation of surface solar radiation. Meanwhile, the low PBL height may limit the vertical exchange of water vapor between the moister surface
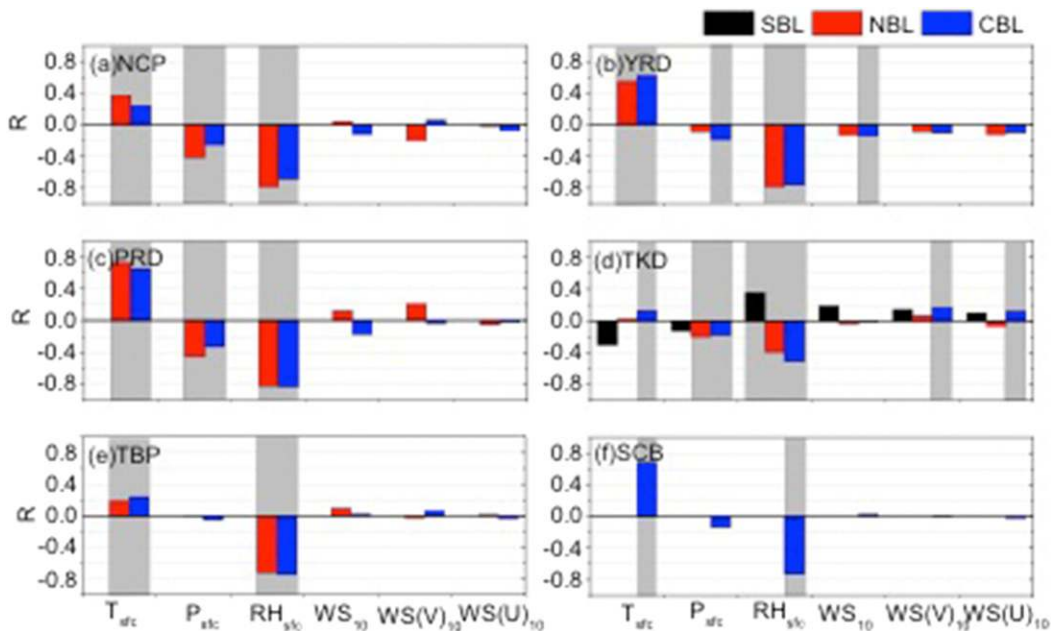

FIG. 9. The correlation coefficients of PBL heights and meteorological parameters in (a)–(f) six ROIs under SBL (black), NBL (red), and CBL (blue) conditions. The meteorological variables are surface temperature T_{sfc}, surface pressure P_{sfc}, surface relatively humidity RH_{sfc}, 10-m wind speed WS_{10}, V component of 10-m wind speed $WS(V)_{10}$, and U component of 10-m wind speed $WS(U)_{10}$. The gray shadings indicate correlations that are statistically significant at the 95% confidence level.
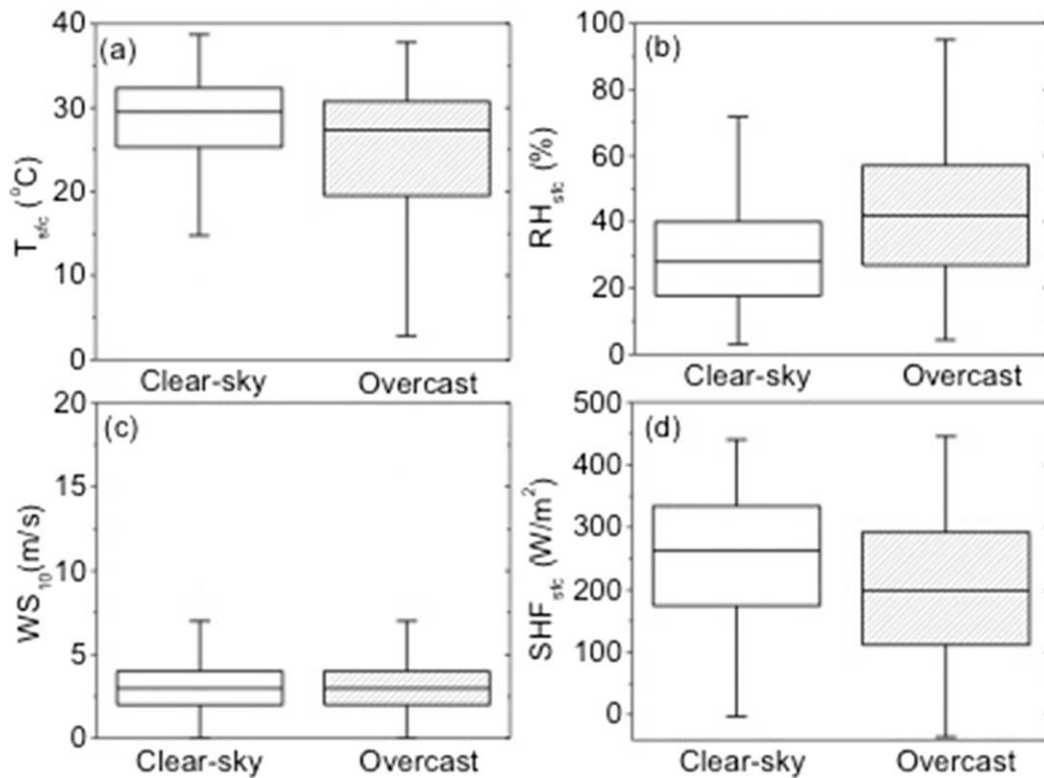
FIG. 10. As in Fig. 8, but comparing the meteorological factors between clear-sky days and overcast days. Note that only the radiosonde sites that have more than 30 observations for both clear-sky and overcast days were considered.

layer and upper drier free troposphere, leading to the relatively high RH_{sfc} (Hohenegger et al. 2009; Zhou and Geerts 2013).

In addition, the soil moisture may be another important factor dictating the development of PBL, since it affects the land surface energy budget (e.g., surface sensible heat flux and latent heat flux). For a specific location, the lower soil moisture generally comes with high surface sensible heat flux, which facilitates the PBL development in the afternoon (McCumber and Pielke 1981; Sanchez-Mejia and Papuga 2014; Rihani et al. 2015). As illustrated in Fig. S4, the northwest of China is mainly covered by bare land, characterized by low soil moisture, high SHF_{sfc}, high Bowen ratio, and low latent heat flux, all of which favors the development of PBL. On the contrary, the high soil moisture, high latent heat flux, low SHF_{sfc}, and low Bowen ratio in southern China are unfavorable to the development of PBL. Furthermore, the high latent heat flux tends to favor cloud formation, and the increased clouds will in turn results in reduced surface temperature, increased soil moisture, and decreased PBL height (Betts et al. 1996; Eltahir 1998; Pal and Eltahir 2001; Zhou and Geerts 2013). Additionally, the different land covers in the northwest

and southeast of China may also play a role in modulating the land surface processes and PBL development. The complex relationships–connections between the land surface properties and PBL in China need more studies in the future.

5. Conclusions

Based on the 1400 BJT soundings in summer collected from the CMA radiosonde network across China from 2012 to 2016, this study investigated the occurrence frequency and spatial distribution of different PBL types (i.e., SBL, NBL, and CBL) in China. In addition, the relationships between the PBL heights and other meteorological variables were examined, including CLD, T_{sfc}, P_{sfc}, RH_{sfc}, and WS_{10}.

The occurrence frequency of CBL is about 70%, followed by 26% for NBL, and 4% for SBL. At 1400 BJT, the spatial distributions of PBL heights for NBL and CBL are quite similar, demonstrating a prominent north–south gradient of PBL height. The depth of SBL (152 ± 100 m) is generally lower than those of NBL (1656 ± 562 m) and CBL (1803 ± 550 m). At 1400 BJT, clouds tend to reduce the occurrence frequency of CBL

and NBL. In terms of cloud impact on the frequency of SBL, it is found to be merely ~10% under clear-sky conditions, as compared to ~70% under overcast conditions, indicating that clouds are one of the key factors dictating the frequency of SBL. With the exception of the discernible changes in PBL height under overcast conditions relative to the PBL height under clear-sky conditions, the PBL height under partly cloudy conditions does not change much (<170 m) under CBL and NBL regimes. This indicates that high cloud cover could be an important factor modulating PBL development. Also, the PBL heights of CBL and NBL were found to be positively correlated with the near-surface meteorological factors such as T_{sfc} but negatively associated with RH_{sfc}. For a specific location, the low RH_{sfc} usually accompanies low CLD and low soil moisture, which could favor the development of PBL in the afternoon with high surface sensible heat flux.

Although the CBL dominates over China in the summer afternoon, the NBL and SBL could also be established and cannot be overlooked. This study merely investigated the afternoon PBL in summer; more efforts should be made to expand the climatology of different PBL types to other seasons in China when more sounding data are available in the future.

REFERENCES

Amenu, G. G., P. Kumar, and X. Z. Liang, 2005: Interannual variability of deep-layer hydrologic memory and mechanisms of its influence on surface energy fluxes. *J. Climate*, **18**, 5024–5045, https://doi.org/10.1175/JCLI3590.1.

Argentini, S., A. Viola, A. Sempreviva, and I. Petenko, 2005: Summer boundary-layer height at the plateau site of Dome'C, Antarctica. *Bound.-Layer Meteor.*, **115**, 409–422, https://doi.org/10.1007/s10546-004-5643-6.

Asimakopoulos, D., C. Helmis, and J. Michopoulos, 2004: Evaluation of SODAR methods for the determination of the atmospheric boundary layer mixing height. *Meteor. Atmos. Phys.*, **85**, 85–92, https://doi.org/10.1007/s00703-003-0036-9.

Betts, A. K., J. H. Ball, A. C. M. Beljaars, M. J. Miller, and P. A. Viterbo, 1996: The land surface-atmosphere interaction: A review based on observational and global modeling perspectives. *J. Geophys. Res.*, **101**, 7209–7225, https://doi.org/10.1029/95JD02135.

——, A. B. Tawfik, and R. L. Desjardins, 2017: Revisiting hydrometeorology using cloud and climate observations. *J. Hydrometeor.*, **18**, 939–955, https://doi.org/10.1175/JHM-D-16-0203.1.

Beyrich, F., 1997: Mixing height estimation from sodar data—A critical discussion. *Atmos. Environ.*, **31**, 3941–3953, https://doi.org/10.1016/S1352-2310(97)00231-8.

Bian, J., H. Chen, H. Vömel, Y. Duan, Y. Xuan, and D. Lü, 2011: Intercomparison of humidity and temperature sensors: GTS1, Vaisala RS80, and CFH. *Adv. Atmos. Sci.*, **28**, 139–146, https://doi.org/10.1007/s00376-010-9170-8.

Blay-Carreras, E., and Coauthors, 2014: Role of the residual layer and large-scale subsidence on the development and evolution of the convective boundary layer. *Atmos. Chem. Phys.*, **14**, 4515–4530, https://doi.org/10.5194/acp-14-4515-2014.

Bonner, W. D., 1968: Climatology of the low level jet. *Mon. Wea. Rev.*, **96**, 833–850, https://doi.org/10.1175/1520-0493(1968)096<0833:COTLLJ>2.0.CO;2.

Chan, K. M., and R. Wood, 2013: The seasonal cycle of planetary boundary layer depth determined using COSMIC radio occultation data. *J. Geophys. Res. Atmos.*, **118**, 12 422–12 434, https://doi.org/10.1002/2013JD020147.

Chen, F., and J. Dudhia, 2001: Coupling an advanced land surface–hydrology model with the Penn State–NCAR MM5 modeling system. Part I: Model implementation and sensitivity. *Mon. Wea. Rev.*, **129**, 569–585, https://doi.org/10.1175/1520-0493(2001)129<0569:CAALSH>2.0.CO;2.

Chen, S. S., and R. A. Houze, 1997: Diurnal variation and life-cycle of deep convective systems over the tropical Pacific warm pool. *Quart. J. Roy. Meteor. Soc.*, **123**, 357–388, https://doi.org/10.1002/qj.49712353806.

Coulter, R. L., 1979: A comparison of three methods for measuring mixing-layer height. *J. Appl. Meteor.*, **18**, 1495–1499, https://doi.org/10.1175/1520-0450(1979)018<1495:ACOTMF>2.0.CO;2.

Dandou, A., M. Tombrou, K. Schäfer, S. Emeis, A. P. Protonotariou, E. Bossioli, N. Soulakellis, and P. Suppan, 2009: A comparison between modelled and measured mixing-layer height over Munich. *Bound.-Layer Meteor.*, **131**, 425–440, https://doi.org/10.1007/s10546-009-9373-7.

Davy, R., and I. Esau, 2016: Differences in the efficacy of climate forcings explained by variations in atmospheric boundary layer depth. *Nat. Commun.*, **7**, 11690, https://doi.org/10.1038/ncomms11690.

Dirmeyer, P. A., Z. Wang, M. J. Mbuh, and H. E. Norton, 2014: Intensified land surface control on boundary layer growth in a changing climate. *Geophys. Res. Lett.*, **41**, 1290–1294, https://doi.org/10.1002/2013GL058826.

Eltahir, E. A. B., 1998: A soil moisture–rainfall feedback mechanism. Part I: Theory and observations. *Water Resour. Res.*, **34**, 765–776, https://doi.org/10.1029/97WR03499.

——, and C. Gong, 1996: Dynamics of wet and dry years in West Africa. *J. Climate*, **9**, 1030–1042, https://doi.org/10.1175/1520-0442(1996)009<1030:DOWADY>2.0.CO;2.

Eresmaa, N., A. Karppinen, S. Joffre, J. Räsänen, and H. Talvitie, 2006: Mixing height determination by ceilometer. *Atmos. Chem. Phys.*, **6**, 1485–1493, https://doi.org/10.5194/acp-6-1485-2006.

Esau, I., and S. Zilitinkevich, 2010: On the role of the planetary boundary layer depth in the climate system. *Adv. Sci. Res.*, **4**, 63, https://doi.org/10.5194/asr-4-63-2010.

Fletcher, J., S. Mason, and C. Jakob, 2016: The climatology, meteorology, and boundary layer structure of marine cold air

outbreaks in both hemispheres. *J. Climate*, **29**, 1999–2014, https://doi.org/10.1175/JCLI-D-15-0268.1.

Freedman, J. M., D. R. Fitzjarrald, K. E. Moore, and R. K. Sakai, 2001: Boundary layer clouds and vegetation–atmosphere feedbacks. *J. Climate*, **14**, 180–197, https://doi.org/10.1175/1520-0442(2001)013<0180:BLCAVA>2.0.CO;2.

Garcia-Carreras, L., J. H. Marsham, and D. V. Spracklen, 2017: Observations of increased cloud cover over irrigated agriculture in an arid environment. *J. Hydrometeor.*, **18**, 2161–2172, https://doi.org/10.1175/JHM-D-16-0208.1.

Garratt, J. R., 1992: *The Atmospheric Boundary Layer*. Cambridge University Press, 316 pp.

——, 1994: Review: The atmospheric boundary layer. *Earth-Sci. Rev.*, **37**, 89–134, https://doi.org/10.1016/0012-8252(94)90026-4.

Garreaud, R., and R. C. Muñoz, 2005: The low-level jet off the west coast of subtropical South America: Structure and variability. *Mon. Wea. Rev.*, **133**, 2246–2261, https://doi.org/10.1175/MWR2972.1.

Guo, J., and Coauthors, 2009: Correlation between PM concentrations and aerosol optical depth in eastern China. *Atmos. Environ.*, **43**, 5876–5886, https://doi.org/10.1016/j.atmosenv.2009.08.026.

——, X. Zhang, Y. Wu, Y. Zhaxi, H. Che, B. La, W. Wang, and X. Li, 2011: Spatio-temporal variation trends of satellite-based aerosol optical depth in China during 1980–2008. *Atmos. Environ.*, **45**, 6802–6811, https://doi.org/10.1016/j.atmosenv.2011.03.068.

——, J. He, H. Liu, Y. Miao, H. Liu, and P. Zhai, 2016a: Impact of various emission control schemes on air quality using WRF-Chem during APEC China 2014. *Atmos. Environ.*, **140**, 311–319, https://doi.org/10.1016/j.atmosenv.2016.05.046.

——, and Coauthors, 2016b: The climatology of planetary boundary layer height in China derived from radiosonde and reanalysis data. *Atmos. Chem. Phys.*, **16**, 13 309–13 319, https://doi.org/10.5194/acp-16-13309-2016.

——, and Coauthors, 2016c: Three-dimensional structure of aerosol in China: A perspective from multi-satellite observations. *Atmos. Res.*, **178–179**, 580–589, https://doi.org/10.1016/j.atmosres.2016.05.010.

Hennemuth, B., and A. Lammert, 2006: Determination of the atmospheric boundary layer height from radiosonde and lidar backscatter. *Bound.-Layer Meteor.*, **120**, 181–200, https://doi.org/10.1007/s10546-005-9035-3.

Hirsch, E., I. Koren, O. Altaratz, Z. Levin, and E. Agassi, 2017: Enhanced humidity pockets originating in the mid boundary layer as a mechanism of cloud formation below the lifting condensation level. *Environ. Res. Lett.*, **12**, 024020, https://doi.org/10.1088/1748-9326/aa5ba4.

Hohenegger, C., P. Brockhaus, C. S. Bretherton, and C. Schar, 2009: The soil moisture–precipitation feedback in simulations with explicit and parameterized convection. *J. Climate*, **22**, 5003–5020, https://doi.org/10.1175/2009JCLI2604.1.

Holzworth, G. C., 1964: Estimates of mean maximum mixing depths in the contiguous United States. *Mon. Wea. Rev.*, **92**, 235–242, https://doi.org/10.1175/1520-0493(1964)092<0235:EOMMMD>2.3.CO;2.

Hoover, J. D., D. R. Stauffer, S. J. Richardson, L. Mahrt, B. J. Gaudet, and A. Suarez, 2015: Submeso motions within the stable boundary layer and their relationships to local indicators and synoptic regime in moderately complex terrain. *J. Appl. Meteor. Climatol.*, **54**, 352–369, https://doi.org/10.1175/JAMC-D-14-0128.1.

Hu, X., G. Nielsen, W. John, and F. Zhang, 2010: Evaluation of three planetary boundary layer schemes in the WRF model. *J. Appl. Meteor. Climatol.*, **49**, 1831–1844, https://doi.org/10.1175/2010JAMC2432.1.

Huang, J., Q. Fu, J. Su, Q. Tang, P. Minnis, Y. Hu, Y. Yi, and Q. Zhao, 2009: Taklimakan dust aerosol radiative heating derived from CALIPSO observations using the Fu-Liou radiation model with CERES constraints. *Atmos. Chem. Phys.*, **9**, 4011–4021, https://doi.org/10.5194/acp-9-4011-2009.

Keyser, D., and R. A. Anthes, 1982: The influence of planetary boundary layer physics on frontal structure in the Hoskins-Bretherton horizontal shear model. *J. Atmos. Sci.*, **39**, 1783–1802, https://doi.org/10.1175/1520-0469(1982)039<1783:TIOPBL>2.0.CO;2.

Lammert, A., and J. Bösenberg, 2006: Determination of the convective boundary-layer height with laser remote sensing. *Bound.-Layer Meteor.*, **119**, 159–170, https://doi.org/10.1007/s10546-005-9020-x.

Li, Z., and Coauthors, 2017: Aerosol and boundary-layer interactions and impact on air quality. *Natl. Sci. Rev.*, nwx117, https://doi.org/10.1093/nsr/nwx117.

Lin, Y., Y. Wang, R. Zhang, and Y. Liu, 2016: Response of boundary layer clouds to continental pollution during the RACORO campaign. *J. Atmos. Sci.*, **73**, 3681–3700, https://doi.org/10.1175/JAS-D-15-0361.1.

Liu, J., J. Huang, B. Chen, T. Zhou, H. Yan, H. Jin, Z. Huang, and B. Zhang, 2015: Comparisons of PBL heights derived from CALIPSO and ECMWF reanalysis data over China. *J. Quant. Spectrosc. Radiat. Transfer*, **153**, 102–112, https://doi.org/10.1016/j.jqsrt.2014.10.011.

Liu, S., and X.-Z. Liang, 2010: Observed diurnal cycle climatology of planetary boundary layer height. *J. Climate*, **23**, 5790–5809, https://doi.org/10.1175/2010JCLI3552.1.

——, X. Yue, F. Hu, and H. Liu, 2004: Using a Modified Soil-Plant-Atmosphere Scheme (MSPAS) to simulate the interaction between land surface processes and atmospheric boundary layer in semi-arid regions. *Adv. Atmos. Sci.*, **21**, 245–259, https://doi.org/10.1007/BF02915711.

Ma, Y., W. Yao, and B. Huang, 2011: Comparison of temperature and geopotential height records between 59 type and L-band radiosonde systems. *J. Appl. Meteor. Sci.*, **22**, 336–345.

Mao, M., W. Jiang, J. Gu, C. Xie, and J. Zhou, 2009: Study on the mixed layer, entrainment zone, and cloud feedback based on lidar exploration of Nanjing city. *Geophys. Res. Lett.*, **36**, L04808, https://doi.org/10.1029/2008GL036768.

McCumber, M. C., and R. A. Pielke, 1981: Simulation of the effects of surface fluxes of heat and moisture in a mesoscale numerical model: 1. Soil layer. *J. Geophys. Res.*, **86**, 9929–9938, https://doi.org/10.1029/JC086iC10p09929.

McGrath-Spangler, E. L., and A. S. Denning, 2012: Estimates of North American summertime planetary boundary layer depths derived from space-borne lidar. *J. Geophys. Res.*, **117**, D15101, https://doi.org/10.1029/2012JD017615.

Medeiros, B., A. Hall, and B. Stevens, 2005: What controls the mean depth of the PBL? *J. Climate*, **18**, 3157–3172, https://doi.org/10.1175/JCLI3417.1.

Miao, Y., X. Hu, S. Liu, T. Qian, M. Xue, Y. Zheng, and S. Wang, 2015a: Seasonal variation of local atmospheric circulations and boundary layer structure in the Beijing-Tianjin-Hebei region and implications for air quality. *J. Adv. Model. Earth Syst.*, **7**, 1602–1626, https://doi.org/10.1002/2015MS000522.

——, S. Liu, Y. Zheng, S. Wang, Z. Liu, and B. Zhang, 2015b: Numerical study of the effects of planetary boundary layer structure on the pollutant dispersion within built-up areas. *J. Environ. Sci.*, **32**, 168–179, https://doi.org/10.1016/j.jes.2014.10.025.

——, J. Guo, S. Liu, H. Liu, Z. Li, W. Zhang, and P. Zhai, 2017: Classification of summertime synoptic patterns in Beijing and

their association with boundary layer structure affecting aerosol pollution. *Atmos. Chem. Phys.*, **17**, 3097–3110, https://doi.org/10.5194/acp-17-3097-2017.

Oke, T. R., 2002: *Boundary Layer Climates.* Routledge, 435 pp.

Pal, J. S., and E. A. B. Eltahir, 2001: Pathways relating soil moisture conditions to future summer rainfall within a model of the land–atmosphere system. *J. Climate*, **14**, 1227–1242, https://doi.org/10.1175/1520-0442(2001)014<1227:PRSMCT>2.0.CO;2.

Paluch, I. R., and D. H. Lenschow, 1991: Stratiform cloud formation in the marine boundary layer. *J. Atmos. Sci.*, **48**, 2141–2158, https://doi.org/10.1175/1520-0469(1991)048<2141:SCFITM>2.0.CO;2.

Poulos, G. S., and Coauthors, 2002: CASES-99: A comprehensive investigation of the stable nocturnal boundary layer. *Bull. Amer. Meteor. Soc.*, **83**, 555–581, https://doi.org/10.1175/1520-0477(2002)083<0555:CACIOT>2.3.CO;2.

Rihani, J. F., F. K. Chow, and R. M. Maxwell, 2015: Isolating effects of terrain and soil moisture heterogeneity on the atmospheric boundary layer: Idealized simulations to diagnose land-atmosphere feedbacks. *J. Adv. Model. Earth Syst.*, **7**, 915–937, https://doi.org/10.1002/2014MS000371.

Rodell, M., and Coauthors, 2004: The Global Land Data Assimilation System. *Bull. Amer. Meteor. Soc.*, **85**, 381–394, https://doi.org/10.1175/BAMS-85-3-381.

Sanchez-Mejia, Z. M., and S. A. Papuga, 2014: Observations of a two-layer soil moisture influence on surface energy dynamics and planetary boundary layer characteristics in a semiarid shrubland. *Water Resour. Res.*, **50**, 306–317, https://doi.org/10.1002/2013WR014135.

Sandip, P., and H. Martial, 2015: Forcing mechanisms governing diurnal, seasonal, and interannual variability in the boundary layer depths: Five years of continuous lidar observations over a suburban site near Paris. *J. Geophys. Res. Atmos.*, **120**, 11 936–11 956, https://doi.org/10.1002/2015JD023268.

Sawyer, V., and Z. Li, 2013: Detection, variations and intercomparison of the planetary boundary layer depth from radiosonde, lidar and infrared spectrometer. *Atmos. Environ.*, **79**, 518–528, https://doi.org/10.1016/j.atmosenv.2013.07.019.

Seibert, P., 2000: Review and intercomparison of operational methods for the determination of the mixing height. *Atmos. Environ.*, **34**, 1001–1027, https://doi.org/10.1016/S1352-2310(99)00349-0.

Seidel, D. J., C. O. Ao, and K. Li, 2010: Estimating climatological planetary boundary layer heights from radiosonde observations: Comparison of methods and uncertainty analysis. *J. Geophys. Res.*, **115**, D16113, https://doi.org/10.1029/2009JD013680.

——, Y. Zhang, A. Beljaars, J. C. Golaz, A. R. Jacobson, and B. Medeiros, 2012: Climatology of the planetary boundary layer over the continental United States and Europe. *J. Geophys. Res.*, **117**, D17106, https://doi.org/10.1029/2012JD018143.

Sherwood, S. C., S. Bony, and J. L. Dufresne, 2014: Spread in model climate sensitivity traced to atmospheric convective mixing. *Nature*, **505**, 37–42, https://doi.org/10.1038/nature12829.

Sivaraman, C., S. McFarlane, E. Chapman, M. Jensen, T. Toto, S. Liu, and M. Fischer, 2013: Planetary boundary layer (PBL) height value added product (VAP): Radiosonde retrievals. U.S. Department of Energy Rep. DOE/SC-ARM-TR-132, 36 pp., https://www.arm.gov/publications/tech_reports/doe-sc-arm-tr-132.pdf.

Solomon, A., M. D. Shupe, and N. B. Miller, 2017: Cloud–atmospheric boundary layer–surface interactions on the Greenland Ice Sheet during the July 2012 extreme melt event. *J. Climate*, **30**, 3237–3252, https://doi.org/10.1175/JCLI-D-16-0071.1.

Steyn, D. G., M. Baldi, and R. Hoff, 1999: The detection of mixed layer depth and entrainment zone thickness from lidar backscatter profiles. *J. Atmos. Oceanic Technol.*, **16**, 953–959, https://doi.org/10.1175/1520-0426(1999)016<0953:TDOMLD>2.0.CO;2.

Stull, R. B., 1988: *An Introduction to Boundary Layer Meteorology.* Kluwer, 670 pp.

Sun, J., and Coauthors, 2002: Intermittent turbulence associated with a density current passage in the stable boundary layer. *Bound.-Layer Meteor.*, **105**, 199–219, https://doi.org/10.1023/A:1019969131774.

Tang, G., X. Zhu, B. Hu, J. Xin, L. Wang, C. Münkel, G. Mao, and Y. Wang, 2015: Impact of emission controls on air quality in Beijing during APEC 2014: Lidar ceilometer observations. *Atmos. Chem. Phys.*, **15**, 12 667–12 680, https://doi.org/10.5194/acp-15-12667-2015.

——, and Coauthors, 2016: Mixing layer height and its implications for air pollution over Beijing. *Atmos. Chem. Phys.*, **16**, 2459–2475, https://doi.org/10.5194/acp-16-2459-2016.

Tao, S., X. Chen, and J. Gong, 2006: Error analyses for temperature of L band radiosonde. *Meteor. Mon.*, **32**, 46–51.

Tokinaga, H., and Coauthors, 2006: Atmospheric sounding over the winter Kuroshio Extension: Effect of surface stability on atmospheric boundary layer structure. *Geophys. Res. Lett.*, **33**, L04703, https://doi.org/10.1029/2005GL025102.

Vogelezang, D., and A. Holtslag, 1996: Evaluation and model impacts of alternative boundary-layer height formulations. *Bound.-Layer Meteor.*, **81**, 245–269, https://doi.org/10.1007/BF02430331.

Wang, X., and K. Wang, 2014: Estimation of atmospheric mixing layer height from radiosonde data. *Atmos. Meas. Tech.*, **7**, 1701–1709, https://doi.org/10.5194/amt-7-1701-2014.

——, and ——, 2016: Homogenized variability of radiosonde-derived atmospheric boundary layer height over the global land surface from 1973 to 2014. *J. Climate*, **29**, 6893–6908, https://doi.org/10.1175/JCLI-D-15-0766.1.

Wetzel, P. J., S. Argentini, and A. Boone, 1996: Role of land surface in controlling daytime cloud amount: Two case studies in the GCIP-SW area. *J. Geophys. Res.*, **101**, 7359–7370, https://doi.org/10.1029/95JD02134.

Whiteman, C. D., and J. C. Doran, 1993: The relationship between overlying synoptic-scale flows and winds within a valley. *J. Appl. Meteor.*, **32**, 1669–1682, https://doi.org/10.1175/1520-0450(1993)032<1669:TRBOSS>2.0.CO;2.

Xing, Y., Z. Zhang, Y. Cao, Y. Li, H. Wang, X. Li, and S. Ma, 2009: Experiment and analysis of GPS radiosonde RS92 performance. *Meteor. Sci. Technol.*, **37**, 336–340.

Xu, W., Y. Guo, B. Huang, and S. Gu, 2007: Analysis of GTS radiosonde humidity sensor testing data and correction of upper-air relative humidity radiosonde data. *Meteor. Sci. Technol.*, **35**, 423–428.

Zhang, W., and Coauthors, 2015: Spatial and temporal variability of aerosol vertical distribution based on lidar observations: A haze case study over Jinhua basin. *Adv. Meteor.*, **2015**, 349592, https://doi.org/10.1155/2015/349592.

——, J. Guo, Y. Miao, H. Liu, Y. Zhang, Z. Li, and P. Zhai, 2016: Planetary boundary layer height from CALIOP compared to radiosonde over China. *Atmos. Chem. Phys.*, **16**, 9951–9963, https://doi.org/10.5194/acp-16-9951-2016.

Zhang, Y., D. J. Seidel, J. C. Golaz, C. Deser, and R. A. Tomas, 2011: Climatological characteristics of Arctic and Antarctic surface-based inversions. *J. Climate*, **24**, 5167–5186, https://doi.org/10.1175/2011JCLI4004.1.

——, ——, and S. Zhang, 2013: Trends in planetary boundary layer height over Europe. *J. Climate*, **26**, 10 071–10 076, https://doi.org/10.1175/JCLI-D-13-00108.1.

——, S. Zhang, C. Huang, K. Huang, Y. Gong, and Q. Gan, 2014: Diurnal variations of the planetary boundary layer height estimated from intensive radiosonde observations over Yichang, China. *Sci. China Technol. Sci.*, **57**, 2172–2176, https://doi.org/10.1007/s11431-014-5639-5.

——, and Coauthors, 2018: The climatology of cloud-base height from long-term radiosonde measurements in China. *Adv. Atmos. Sci.*, https://doi.org/10.1007/s00376-017-7096-0, in press.

Zhou, X., and B. Geerts, 2013: The influence of soil moisture on the planetary boundary layer and on cumulus convection over an isolated mountain. Part I: Observations. *Mon. Wea. Rev.*, **141**, 1061–1078, https://doi.org/10.1175/MWR-D-12-00150.1.